Joint inversion of GPR and ER data

Diego Domenzain, Boise State University; John Bradford, Colorado School of Mines; Jodi Mead, Boise State University*

SUMMARY

Electrical methods are proven tools for successfully imaging the subsurface (Jol, 2008; Knight, 2001). Ground penetrating radar (GPR) is sensitive to electrical permittivity through reflectivity and electrical conductivity through attenuation. Electrical resistivity tomography (ER) is directly sensitive to electrical conductivity. GPR and ER data hold high and low spacial-frequency information respectively of the media of interest. We propose a joint inversion of GPR and ER data to image electrical permittivity and conductivity. The two types of data are inherently linked through Maxwell's equations and work cooperatively to regularize each other while honoring the physics. We first compute sensitivity updates separately for both the GPR and ER data using the adjoint method, and then we sum these updates to account for both types of sensitivities. Our algorithm makes no assumption of the subsurface geometry with the caveat of needing a good initial model. In this work, we test our method with a numerical experiment.

INTRODUCTION

Imaging electrical properties (e.g. electrical permittivity ε and conductivity σ) of the subsurface is widely used for imaging the subsurface (Jol, 2008; Knight, 2001).

GPR is sensitive to electrical permittivity by reflectivity and velocity, and it is also sensitive to electrical conductivity through reflectivity and attenuation. However, if attenuation is strong in the media of interest the observed wavefield might not contain enough information to image either the permittivity or the conductivity.

ER is directly (and only) sensitive to electrical conductivity. However, if the media of interest has low conductivity, the measured data might not have enough information to give a meaningful image.

Fortunately, GPR is sensitive to what ER is not (permittivity) and ER is directly sensitive to what GPR is only sensitive by dim reflections and attenuation (conductivity). Moreover, GPR data gives a higher space-frequency resolution image of the media of interest in contrast with the lower space-frequency image obtained with the ER data.

In order to exploit the complimentary sensitivities of the GPR and ER experiments, we propose an imaging algorithm to recover both permittivity and conductivity of the media of interest by joining the sensitivities of conductivity from both the GPR and ER data in each iteration of the inversion process.

We make the physical assumptions of a isotropic linear media where Ohm's law holds, with no lateral variation in the y coordinate, and with a constant magnetic permeability of μ_o.

We formulate our imaging algorithm by finding parameters ε_*, σ_* that satisfy,

$$\{\varepsilon_*, \sigma_*\} = \arg\min E(\varepsilon,\sigma) \tag{1}$$

where we define E to be the sum,

$$E = E_w(\varepsilon,\sigma\,;\, d_w^o) + E_{dc}(\sigma;\, d_{dc}^o). \tag{2}$$

Both E_w and E_{dc} are the sum squared errors of the synthetic and observed data and d_w^o and d_{dc}^o represent the observed data for the GPR and ER experiment respectively. The subscript $*$ denotes the imaged parameters.

We present a two dimensional joint inversion algorithm and give results with simulated noise free data.

SEPARATE INVERSIONS

In order to optimize (2), we first develop and give individual inversion results by finding an update that minimizes E_w and an update that minimizes E_{dc} independently. We further assume that material properties are independent of frequency, which is not true in general, but forms a starting point for the evaluation of the algorithm.

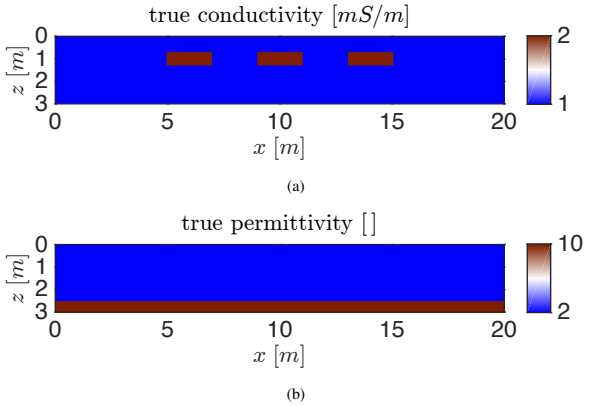

Figure 1: True conductivity and (relative) permittivity used in our numerical experiment. Conductivity anomalies are approximately $\lambda_o \approx 0.4\,m$ tall by $4\lambda_o$ wide and embedded in a homogeneous background conductivity of $1\,mS/m$. The permittivity reflector is also λ_o tall.

GPR sensitivity

The physics of the GPR experiment are given by the time

10.1190/segam2018-2997794.1

dependent Maxwell's equations,

$$\begin{pmatrix} \mu_o & 0 & 0 \\ 0 & \mu_o & 0 \\ 0 & 0 & \varepsilon \end{pmatrix} \begin{pmatrix} \dot{H}_z \\ -\dot{H}_x \\ \dot{E}_y \end{pmatrix} = \begin{pmatrix} 0 & 0 & \partial_x \\ 0 & 0 & \partial_z \\ \partial_x & \partial_z & 0 \end{pmatrix} \begin{pmatrix} H_z \\ -H_x \\ E_y \end{pmatrix} - \sigma \begin{pmatrix} 0 \\ 0 \\ E_y \end{pmatrix} + \begin{pmatrix} 0 \\ 0 \\ -J_y \end{pmatrix}, \tag{3}$$

where E_y is the electric field component in the y direction, (H_x, H_z) are the magnetic field components in the x and z direction, J_y is the source term, M_w is the measuring operator, and $d_w = M_w E_y$ is the data of the experiment (i.e. a shot gather).

In order to find an update direction $\Delta\sigma_w$ that minimizes E_w we follow Ernst et al. (2007) using a full waveform inversion (or adjoint method) approach,

$$\Delta\sigma_w = -\frac{1}{n_w} \sum_{i=1}^{n_w} \alpha_{w,\sigma} g_{w,\sigma}, \tag{4}$$

where n_w is the number of GPR experiments, $g_{w,\sigma}$ is the gradient of E_w with respect to σ for a particular experiment and $\alpha_{w,\sigma}$ is a particular step size for each $g_{w,\sigma}$. A similar equation for $\Delta\varepsilon_w$ follows.

Computing $\alpha_w g_w$ amounts to numerically solving (3) three times: once for the wavefield with current (ε,σ) parameters, once for the backward propagation of errors, and once for the step size α_w as done by Pica et al. (1990). We used a finite difference time domain method on a Yee grid (Yee, 1966) with PML boundary conditions (Berenger, 1994) to solve (3). The update for the conductivity is,

$$\sigma \leftarrow \sigma + \Delta\sigma_w \tag{5}$$

with a similar expression for ε. We performed a numerical example using only GPR data assuming permittivity is known. Five equally spaced shots along the x-axis were fired (source was a Ricker wavelet with center frequency $f_o = 250\,MHz$ and wavelength $\lambda_o \approx 0.4\,m$ at f_o) with λ_o between source and closest receiver, and with subsequent receiver spacing of $\lambda_o/4$. All shots and receivers were placed on the air-ground interface. Figure 1 shows the true model. Figure 2a shows the imaged result.

We note that Figure 2a shows a slight upwards bend in the shape of the anomalies and from the horizontal cross section in Figure 3 we note higher amplitude near the edges of the anomalies.

ER sensitivity

The physics of the ER experiment are given by the steady state Maxwell's equations where Ohm's law holds,

$$-\nabla\cdot\ \sigma\nabla\varphi = \mathbf{i}(\delta(x - s_+) - \delta(x - s_-)), \tag{6}$$

φ is the electric potential, $\mathbf{i}$ is the current intensity, $s_\pm$ is the source-sink position, M_{dc} is the measuring operator that computes observed voltages, and $d_{dc} = M_{dc}\varphi$ is the data of the experiment. Neumann boundary conditions were applied on the air-ground interface, and Robin boundary conditions applied in the subsurface.

To find an update direction $\Delta\sigma_{dc}$ that minimizes E_{dc} we follow the adjoint method (Pidlisecky et al., 2007; Pratt et al., 1998; Domenzain et al., 2017),

$$\Delta\sigma_{dc} = -\frac{1}{n_{dc}} \sum_{i=1}^{n_{dc}} \alpha_{dc} g_{dc}, \tag{7}$$

where n_{dc} is the number of ER experiments, g_{dc} is the gradient of E_{dc} with respect to σ for a particular experiment and α_{dc} is a particular step size for each g_{dc} (Pica et al., 1990).

Similar to the computation of $\alpha_w g_w$, computing $\alpha_{dc} g_{dc}$ amounts to solving equation (6) three times. We used a finite volume method (Dey and Morrison, 1979) to solve (6). The update for the conductivity is,

$$\sigma \leftarrow \sigma + \Delta\sigma_{dc}. \tag{8}$$

We performed a numerical example for a true model as in Figure 1a starting with a homogeneous background conductivity of $1\,mS/m$. We used dipole-dipole and Wenner arrays with an a-spacing ranging from 1 to 6 meters with $1m$ increments. All shots and receivers were placed on the air-ground interface. Figure 2b shows the imaged conductivity.

We note from Figure 2b and Figure 3 that the imaged conductivity gives a slightly smaller magnitude for the anomalies and a very low spacial frequency resolution, i.e. only the broad shape of the anomalies is recovered.

Regularization

Because we are solving for parameters at depth while only acquiring measurements on the air-ground interface, problem (1) is inherently ill posed and regularization is needed. Moreover, computing g_w and g_{dc} using the adjoint method introduces high amplitude artifacts near the receivers (Kurzmann et al., 2013; Taillandier et al., 2009) that dominate the gradients. We follow the approach of Kurzmann et al. (2013) for removing high amplitude artifacts near the receivers on g_w and then the approach of Taillandier et al. (2009) for regularizing both g_{dc} and g_w by applying a space-frequency low-pass gaussian filter $f(\,\cdot\,, k)$ of width k,

$$g_{dc} \leftarrow f(g_{dc}, k_{dc}), \tag{9}$$

with a similar expression for g_w. We choose the width k_{dc} empirically and choose k_w to only allow wavelengths larger or equal to the characteristic wavelength of the not known but sought after target model, i.e. with fixed central frequency f_o and fixed minimum velocity.

JOINT INVERSION

Now that we have our two different updates $\Delta\sigma_w$ and $\Delta\sigma_{dc}$, we propose the update for optimizing (2) as

$$\Delta\sigma = \frac{1}{2}\left(\Delta\sigma_w + \Delta\sigma_{dc}\right), \tag{10}$$

10.1190/segam2018-2997794.1

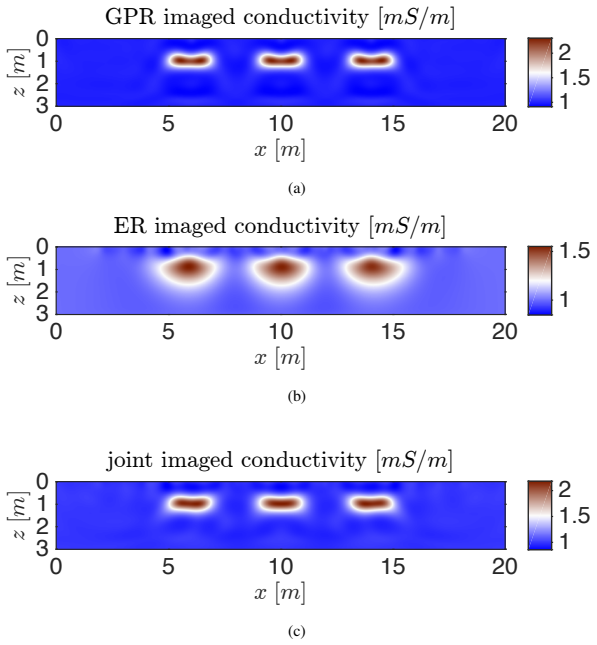

Figure 2: Imaged conductivity using (a) only GPR data, (b) only ER data, (c) our joint inversion algorithm.

and update the conductivity by,

$$\sigma \leftarrow \sigma + \Delta\sigma. \tag{11}$$

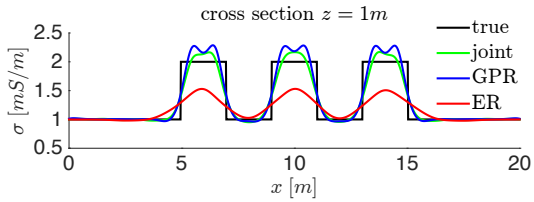

Figure 3: Cross-sections of the true, GPR imaged, ER imaged and joint imaged conductivity.

Example

Figure 2c shows the imaged conductivity using both GPR and ER data from the experiments explained in the previous sections using our joint inversion algorithm with material electrical properties as in Figure 1. Both the GPR and ER numerical models are realized on the same computational grid.

In a realistic scenario, GPR cannot differentiate between reflections from conductivity anomalies or permittivity anomalies. Because the ER experiment is directly sensitive to conductivity, we first image the conductivity using only ER data starting with a homogeneous model $\sigma = 1\,mS/m$. We then use the resulting imaged conductivity (Figure 2b), as an initial guess for our joint inversion.

Because the GPR data is sensitive to higher spatial frequencies than the ER data, Figure 4a displays sharper contrasts

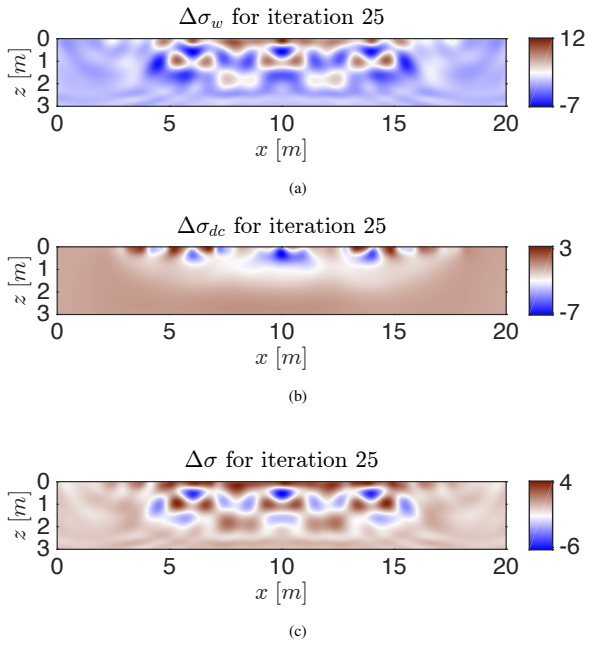

Figure 4: Update snapshots during the joint inversion for iteration 25 as given by (a) equation (4), (b) equation (7) and (c) equation (10).

than Figure 4b. Both for Figure 4a and Figure 4b, not all features will update σ to the true model because our sources and data acquisition are realized only at discrete locations on the air-ground interface. Fortunately, both figures contain complimentary features that correct these artifacts. For example Figure 4a displays a sequence of peak-trough-peak where each true anomaly lies, with each peak and trough roughly of width λ_o. However, Figure 4b dampens these artifacts in favor of a lower space-frequency update direction as can be seen in Figure 4c.

To further observe how space-frequency artifacts are better corrected with our joint inversion algorithm, we refer to Figure 3 where we display the true conductivity together with the separate and joint inversions results. Where the true anomalies are, the GPR imaged conductivity exhibits a sequence of peak-trough-peak, the ER imaged conductivity exhibits a very shallow peak, while the joint imaged conductivity exhibits a more accurate flatter peak.

CONCLUSION

We have developed an imaging algorithm for recovering electrical permittivity and electrical conductivity from the subsurface with no assumed geometry (i.e. layered) by joining sensitivities of GPR and ER data. Our approach enhances the sensitivity of the GPR (and ER) data when the target media has high (or low) conductivity, and it also enhances the spatial resolution of GPR (and ER) by introducing low (and high) spatial frequency information of the subsurface as seen in Figure 2c and Figure 4.

10.1190/segam2018-2997794.1

Given the long offsets and high computational cost needed for both the GPR and ER experiments, our approach is best suited for shallow subsurface investigation. As a caveat, an accurate initial background model for both permittivity and conductivity is needed in both the GPR and ER inversions, which can be solved using reflection tomography of GPR data (Bradford, 2006) and independent ER inversion.

DOI:10.1190/segam2018-2997794.1

10.1190/segam2018-2997794.1

REFERENCES

Berenger, J.-P., 1994, A perfectly matched layer for the absorption of electromagnetic waves: Journal of Computational Physics, **114**, 185–200, https://doi.org/10.1006/jcph.1994.1159.

Bradford, J. H., 2006, Applying reflection tomography in the postmigration domain to multifold ground-penetrating radar data: Geophysics, **71**, no. 1, K1–K8, https://doi.org/10.1190/1.2159051.

Dey, A., and H. Morrison, 1979, Resistivity modelling for arbitrarily shaped two-dimensional structures: Geophysical Prospecting, **27**, 106–136, https://doi.org/10.1111/j.1365-2478.1979.tb00961.x.

Domenzain, D., J. Bradford, and J. Mead, 2017, Imaging by joint inversion of electromagnetic waves and DC currents: Presented at the SIAM Mathematical and Computational issues in the Geosciences.

Ernst, J. R., H. Maurer, A. G. Green, and K. Holliger, 2007, Full-waveform inversion of crosshole radar data based on 2-D finite-difference time-domain solutions of Maxwell's equations: IEEE Transactions on Geoscience and Remote Sensing, **45**, 2807–2828, https://doi.org/10.1109/tgrs.2007.901048.

Jol, H. M., 2008, Ground penetrating radar theory and applications: Elsevier.

Knight, R., 2001, Ground penetrating radar for environmental applications: Annual Review of Earth and Planetary Sciences, **29**, 229–255.

Kurzmann, A., A. Przebindowska, D. Köhn, and T. Bohlen, 2013, Acoustic full waveform tomography in the presence of attenuation: A sensitivity analysis: Geophysical Journal International, **195**, 985–1000, https://doi.org/10.1093/gji/ggt305.

Pica, A., J. Diet, and A. Tarantola, 1990, Nonlinear inversion of seismic reflection data in a laterally invariant medium: Geophysics, **55**, 284–292, https://doi.org/10.1190/1.1442836.

Pidlisecky, A., E. Haber, and R. Knight, 2007, Resinvm3d: A 3D resistivity inversion package: Geophysics, **72**, no. 2, H1–H10.

Pratt, R. G., C. Shin, and G. Hick, 1998, Gauss-Newton and full Newton methods in frequency-space seismic waveform inversion: Geophysical Journal International, **133**, 341–362, https://doi.org/10.1046/j.1365-246x.1998.00498.x.

Taillandier, C., M. Noble, H. Chauris, and H. Calandra, 2009, First-arrival traveltime tomography based on the adjoint-state method: Geophysics, **74**, no. 6, WCB1–WCB10, https://doi.org/10.1190/1.3250266.

Yee, K., 1966, Numerical solution of initial boundary value problems involving Maxwell's equations in isotropic media: IEEE Transactions on Antennas and Propagation, **14**, 302–307, https://doi.org/10.1109/tap.1966.1138693.